Robust zero-energy modes in an electronic higher-order topological insulator

S. N. Kempkes[1,6], M. R. Slot [ID][2,6], J. J. van den Broeke[1], P. Capiod[2], W. A. Benalcazar[3],
D. Vanmaekelbergh[2], D. Bercioux[4,5], I. Swart [ID][2]* and C. Morais Smith [ID][1]*

Quantum simulators are essential tools for understanding complex quantum materials. Platforms based on ultracold atoms in optical lattices and photonic devices have led the field so far, but the basis for electronic quantum simulators is now being developed. Here, we experimentally realize an electronic higher-order topological insulator (HOTI). We create a breathing kagome lattice by manipulating carbon monoxide molecules on a Cu(111) surface using a scanning tunnelling microscope. We engineer alternating weak and strong bonds to show that a topological state emerges at the corner of the non-trivial configuration, but is absent in the trivial one. Different from conventional topological insulators, the topological state has two dimensions less than the bulk, denoting a HOTI. The corner mode is protected by a generalized chiral symmetry, which leads to a particular robustness against perturbations. Our versatile approach to designing artificial lattices holds promise for revealing unexpected quantum phases of matter.

Quantum simulators—systems that can be engineered and manipulated at will—are useful platforms for verifying model Hamiltonians and understanding more complex or elusive quantum systems[1,2]. The simulation of the Bose–Hubbard model and the superfluid–Mott-insulator transition in a two-dimensional (2D) optical lattice loaded with ^{87}Rb atoms opened the path for the use of ultracold atoms as quantum simulators[3]. Since then, triangular, honeycomb, kagome and other types of optical lattices have been loaded with bosons and/or fermions, and many interesting quantum states of matter have been simulated[4]. Quantum simulators were also realized in trapped ion[5] and photonic systems[6], among others. By contrast, progress on electronic systems was achieved only very recently. A few years ago, the first artificial electronic lattice was built by positioning carbon monoxide (CO) molecules on a Cu(111) surface, confining the surface-state electrons to a honeycomb lattice[7]. The technique was inspired by the pioneering construction of quantum corrals using scanning tunnelling microscope (STM)-based manipulations of adatoms[8]. This was followed by other electronic and spin lattices constructed by atomic manipulation in the STM, such as atomic spin chains[9,10], the Lieb lattice with s orbitals[11,12] and p orbitals[13], the quasicrystalline Penrose tiling[14] and the Sierpiński gasket with a fractional dimension[15].

In addition to manipulating the geometry and the dimensionality, it is desirable to engineer and control topological properties[16] in electronic systems. Topological insulators, superconductors and semimetals have attracted enormous attention in recent decades, and their potential use in quantum computers has caused a frantic interest in these systems[17]. In their best known form, topological insulators are materials that are insulating in the bulk and host topologically protected states in one dimension lower than the bulk[18]. A first example of engineered electronic topological insulators established by controlled fabrication on the nanoscale is the one-dimensional (1D) Su–Schrieffer–Heeger (SSH) chain[12]. However, recently it was proposed that another class of topological systems exists, the so-called electronic higher-order topological insulators (HOTIs), in which the topological states emerge in at least two dimensions lower than the bulk[19]. In this way, 0D corner (1D hinge) states were predicted and subsequently observed in a 2D[20] (3D[21]) topological insulator. HOTIs have been experimentally realized in photonic[20,22,23], phononic[24], topolectrical circuit[25], microwave circuit[26] and acoustic[27,28] systems.

Here, we present the artificial realization of an electronic HOTI. Specifically, we create and characterize a breathing kagome lattice[29]. This lattice, shown in Fig. 1a, is described by three sites in a unit cell (grey hexagon) with a nearest-neighbour (NN) intracell hopping t_a and intercell hopping t_b (red and blue lines, respectively). The next-nearest-neighbour (NNN) hopping t_{nnn} is indicated in purple only at the top of the lattice (for clarity). In our finite triangular lattice, the corner sites are represented by a blue colour, whereas the edge sites are indicated in yellow and the bulk sites in green. The Bloch Hamiltonian (without NNN hopping) of this model reads

$$h_K(\mathbf{k}) = - \begin{pmatrix} -\varepsilon & t_a + t_b e^{i\mathbf{k}\cdot\mathbf{a}_2} & t_a + t_b e^{-i\mathbf{k}\cdot\mathbf{a}_3} \\ t_a + t_b e^{-i\mathbf{k}\cdot\mathbf{a}_2} & -\varepsilon & t_a + t_b e^{-i\mathbf{k}\cdot\mathbf{a}_1} \\ t_a + t_b e^{i\mathbf{k}\cdot\mathbf{a}_3} & t_a + t_b e^{i\mathbf{k}\cdot\mathbf{a}_1} & -\varepsilon \end{pmatrix} \quad (1)$$

where ε is the on-site energy, $\mathbf{k}$ the crystal momentum, and $\mathbf{a}_1 = (1, 0)$ and $\mathbf{a}_{2,3} = \left(\frac{1}{2}, \pm\frac{\sqrt{3}}{2}\right)$ are the lattice vectors. The full tight-binding Hamiltonian that describes the experimentally realized lattice is given in the Supplementary Information. The bulk band structure is shown in Fig. 1b. The regular kagome lattice exhibits a spectrum with a Dirac cone and a flat band. The alternating hopping strengths in the breathing kagome lattice $t_a \neq t_b$ open a bandgap between the bottom and middle bands at the K-point, as displayed for realistic values $t_a = 28.5$ meV and $t_b = 75$ meV. The otherwise flat top band is dispersive due to a non-negligible $t_{nnn} = 8.8$ meV (see Methods and Supplementary Information).

[1]Institute for Theoretical Physics, Utrecht University, Utrecht, the Netherlands. [2]Debye Institute for Nanomaterials Science, Utrecht University, Utrecht, the Netherlands. [3]Department of Physics, The Pennsylvania State University, University Park, PA, USA. [4]Donostia International Physics Center, San Sebastian, Spain. [5]IKERBASQUE, Basque Foundation of Science, Bilbao, Spain. [6]These authors contributed equally: S. N. Kempkes, M. R. Slot.
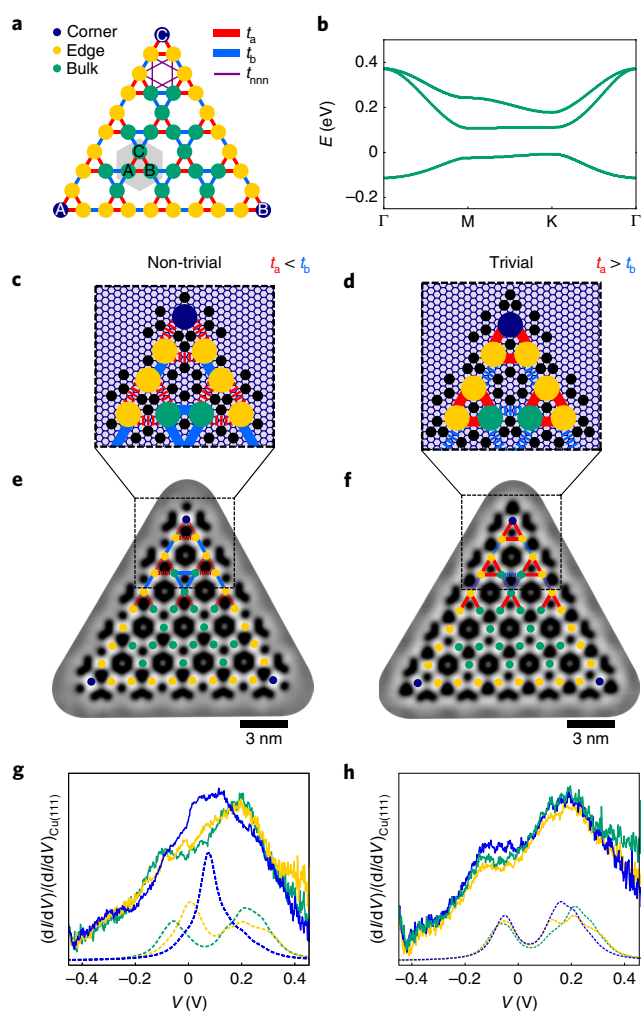*e-mail: I.Swart@uu.nl; C.deMoraisSmith@uu.nl

Fig. 1 | Design of the breathing kagome lattice. a, Schematic representation of the finite-size breathing kagome lattice, consisting of three sublattices A, B and C. The unit cell is indicated by a grey hexagon. The tight-binding hopping parameters t_a, t_b and t_{nnn} are indicated by red, blue and purple, respectively. **b**, Band structure for the bulk of the lattice shown in **a**, calculated using a tight-binding model with $t_b = 75\,\text{meV}$, $t_a = 0.38t_b$, $t_{nnn} = 0.25t_b$ and $\varepsilon = 0.075\,\text{eV}$. **c,d**, Configuration of CO molecules (black) on a Cu(111) surface (grey background) to establish artificial lattice sites (blue, yellow and green) in a non-trivial ($t_a < t_b$) (**c**) and trivial ($t_a > t_b$) (**d**) breathing kagome geometry, respectively. Smaller (larger) hopping is indicated by dashed (solid) lines. **e,f**, Constant-current STM images of the realized non-trivial (**e**) and trivial (**f**) kagome lattices. Imaging parameters: $I = 0.3\,\text{nA}$ and $I = 0.1\,\text{nA}$, respectively, and $V = 100\,\text{mV}$. **g,h**, Normalized differential conductance spectra (solid lines) and the LDOS calculated using the tight-binding model (dashed lines) for the bulk (green), edge (yellow) and corner (blue) sites of the non-trivial (**g**) and trivial (**h**) breathing kagome lattices, respectively.

For the finite-sized lattice, we distinguish two cases. If $t_a > t_b$, the lattice configuration is topologically trivial; if the values of the hopping amplitudes are switched, that is $t_a < t_b$, the lattice is topologically non-trivial. In the topological phase, the weakly coupled edge and corner sites are predicted to accommodate edge states and zero-energy corner modes[29,30], respectively. The edge of the lattice is similar to a 1D SSH model and exhibits gapped bands. In the gap of both the bulk and the edge, three symmetry-protected zero-energy modes arise, which are localized at each of the corners of the lattice.

Usually, the protection of zero-energy topological states is possible in insulators or superconductors that exhibit a symmetric spectrum. In topological superconductors, the particle-hole symmetry enforces this spectral symmetry and pins the energies of Majorana bound states exactly at zero energy in its Bogoliubov–de Gennes spectrum. In insulators, bipartite lattices provide such spectral symmetry. The bipartite character of a crystal, often known as chiral symmetry, protects an integer number of zero-energy states in 1D systems such as the SSH model (see Supplementary Information). Recently it was shown that when additional crystalline symmetries are present, bipartite lattices can also protect zero-energy corner states in 2D HOTIs[20]. The kagome lattice, however, is not a bipartite lattice but consists of three sublattices A, B and C (see unit cell in Fig. 1a). This poses a conundrum because this lattice exhibits higher-order zero-energy states at 60° corners in the topological configuration, despite the absence of the chiral symmetry associated with bipartite lattices. The protection of these zero-energy corner states can be explained by a generalized chiral symmetry, which relies on the fact that the kagome lattice is tripartite[28] (see Supplementary Information).

Now we turn to the experimental realization of the electronic breathing kagome lattice. Figure 1c,d presents the configuration of CO molecules (black) on Cu(111) (grey background) used to constrain the surface-state electrons to the non-trivial and trivial lattice geometry, respectively. Since the CO molecules act as a repulsive barrier to the 2D electron gas at the Cu(111) surface, they are positioned to form the anti-lattice of the kagome. The distance between the artificial lattice sites of the kagome lattice is chosen to be $3\sqrt{3}a \approx 13.3\,\text{Å}$, where $a \approx 2.56\,\text{Å}$ denotes the Cu(111) NN distance. Strong hopping (solid lines) is established by a wide connection between the sites, while the hopping is weaker (dashed lines) for a narrow connection, implemented by an increased number of CO adsorbates. The experimental realization of the non-trivial and trivial breathing kagome lattice is shown in the constant-current STM images in Fig. 1e,f. As a guide to the eye, the artificial lattice sites and the NN hopping are indicated. Differential conductance spectra were acquired above the bulk (green), edge (yellow) and corner (blue) artificial lattice sites and normalized by the average spectrum taken on clean Cu(111)[7]. We first discuss the spectra acquired above the non-trivial lattice (see Fig. 1g, solid lines). The bulk spectrum (green) shows a peak around a bias voltage of $V = -150\,\text{mV}$, which corresponds to the lowest bulk band, and a more pronounced peak around $V = +200\,\text{mV}$, which can be assigned to the middle and top bulk bands. The edge spectrum (yellow) exhibits two peaks located around $V = -20\,\text{mV}$ and $V = +200\,\text{mV}$, indicating two edge modes. This resembles an SSH chain at the edge with two bands, of which the top band minimum and bottom band maximum are separated by $2(t_b - t_a)$ (without orbital overlap). Around $V = +75\,\text{mV}$, a minimum of the bulk and edge spectra, the corner spectrum (blue) exhibits a maximum. Since there is no on-site potential disorder in the artificial lattice due to the atomic precision that we achieve in its construction, we attribute this peak to zero-energy modes localized at the corners, which are protected by a generalized chiral symmetry. Note that this maximum is located at $\varepsilon = 0.075\,\text{eV}$, which denotes the 'zero-energy' of this system. In contrast to the non-trivial lattice, the spectra of bulk, edge and corner sites of the trivial lattice are similar (see Fig. 1h, solid lines). These results indicate the presence of an electronic zero mode in the non-trivial breathing kagome lattice. The differential conductance spectra are reproduced by tight-binding calculations of the local density of states (LDOS) at the designated artificial lattice sites, displayed underneath the experimental spectra in Fig. 1g,h (dashed lines), with the same hopping parameters as used in Fig. 1b. The results are further corroborated by muffin-tin calculations (see Supplementary Information).

In Fig. 2, we investigate the spatial LDOS at bias voltages corresponding to the peak positions in the differential conductance
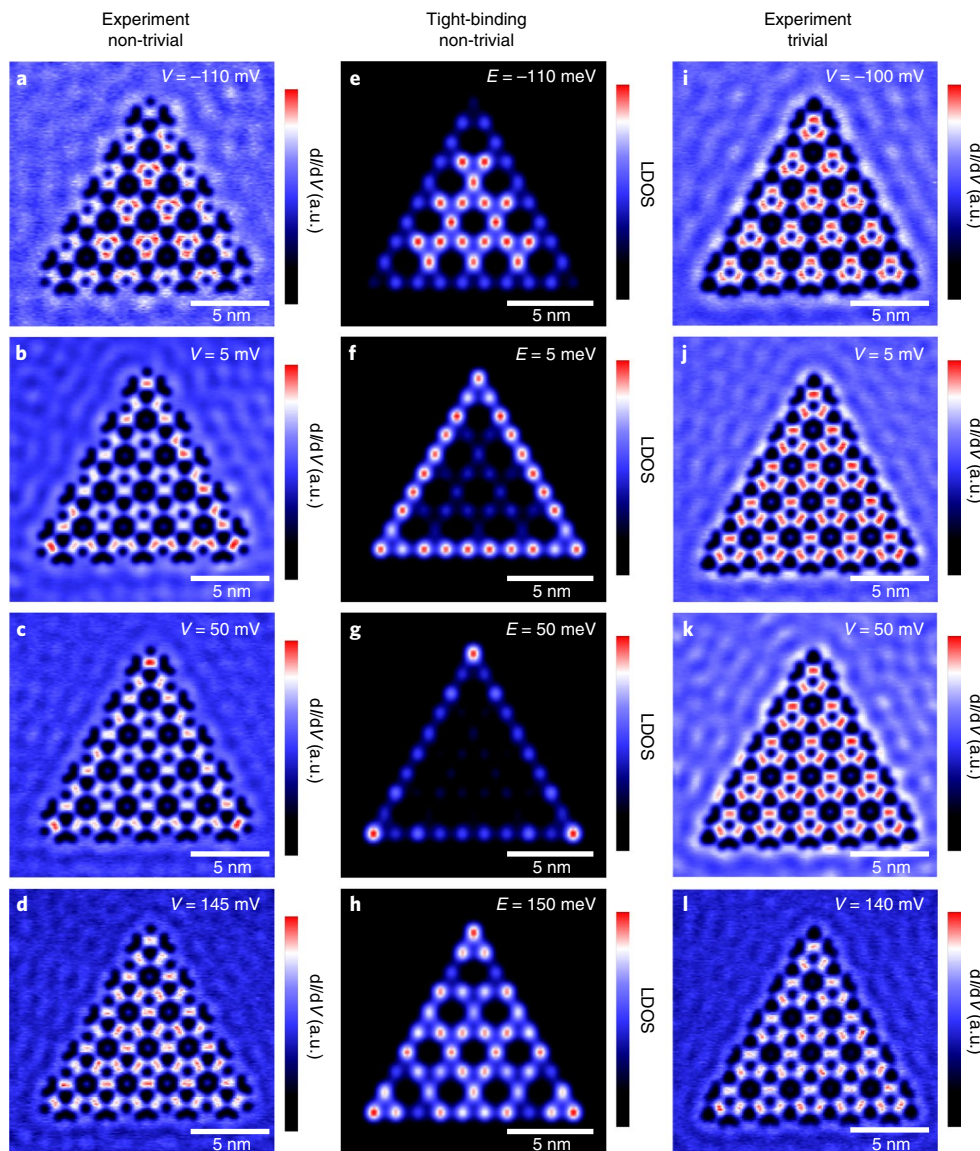
Fig. 2 | Wave function mapping. a–d, Differential conductance maps acquired above the non-trivial breathing kagome lattice at $V = -110$ mV (**a**), $V = +5$ mV (**b**), $V = +50$ mV (**c**) and $V = +145$ mV (**d**). The standing waves around the lattice originate from scattering of the 2D electron gas outside of the lattice with the kagome geometry[8]. **e–h**, LDOS maps of the non-trivial lattice at similar energies, simulated using the tight-binding model. **i–l**, Differential conductance maps acquired above the trivial lattice at values of V similar to those in **a–d**.

spectra. Differential conductance maps acquired above the non-trivial lattice (Fig. 2a–d) are compared with tight-binding calculations (Fig. 2e–h) and differential conductance maps of the trivial lattice (Fig. 2i–l). At $V = -110$ mV, the electrons are localized in the bulk of the non-trivial kagome lattice. Next, at $V = +5$ meV, the contribution of the bottom edge band is visible. At $V = +50$ mV, we observe the highest intensity at the weakly connected corner sites, revealing the corner-localized zero modes. Finally, at $V = +145$ mV, all sites exhibit a similar LDOS, as expected from the spectra. These results are in agreement with the tight-binding simulations on the non-trivial lattice (Fig. 2e–h). In contrast, the differential conductance maps obtained above the trivial lattice show a homogeneous LDOS at all bias voltages. In particular, the corner sites do not exhibit a higher intensity than the other sites at $V = +50$ mV. The shift of the electron probability from the centre to the edges and then finally to the corner sites is only seen for the non-trivial lattice and fully corroborated by tight-binding and muffin-tin calculations (see Supplementary Information).

The zero modes in the kagome lattice are protected by the generalized chiral symmetry[28] (see Methods and Supplementary Information). To investigate their robustness, we perform tight-binding calculations including only t_a and t_b, and we set $t_{nnn} = 0$ for simplicity. Furthermore, we set $\varepsilon = 0$ because there is no on-site potential disorder among different sites in the experimental lattice. We now focus on the top of the lattice, where the corner mode is localized on the sublattice C. Figure 3a shows that this zero mode has support only on the C sublattice and decays exponentially in the neighbouring C sites in the bulk and at the edge (the size of the dots represents $|\psi|^{0.2}$ to allow for a visualization of the decay of the wave function; see the Supplementary Information for the exponential decay of the wave function). If we now locally break the chiral symmetry by introducing a small hopping $t_2 = 0.05t_b$, connecting the A–A and the B–B sites in the neighbourhood of the top corner, the zero mode in C remains unperturbed (see Fig. 3b). However, if we connect C–C neighbours by a hopping t_2, thus locally breaking the chiral symmetry of the C sublattice, the zero mode in C loses protection,
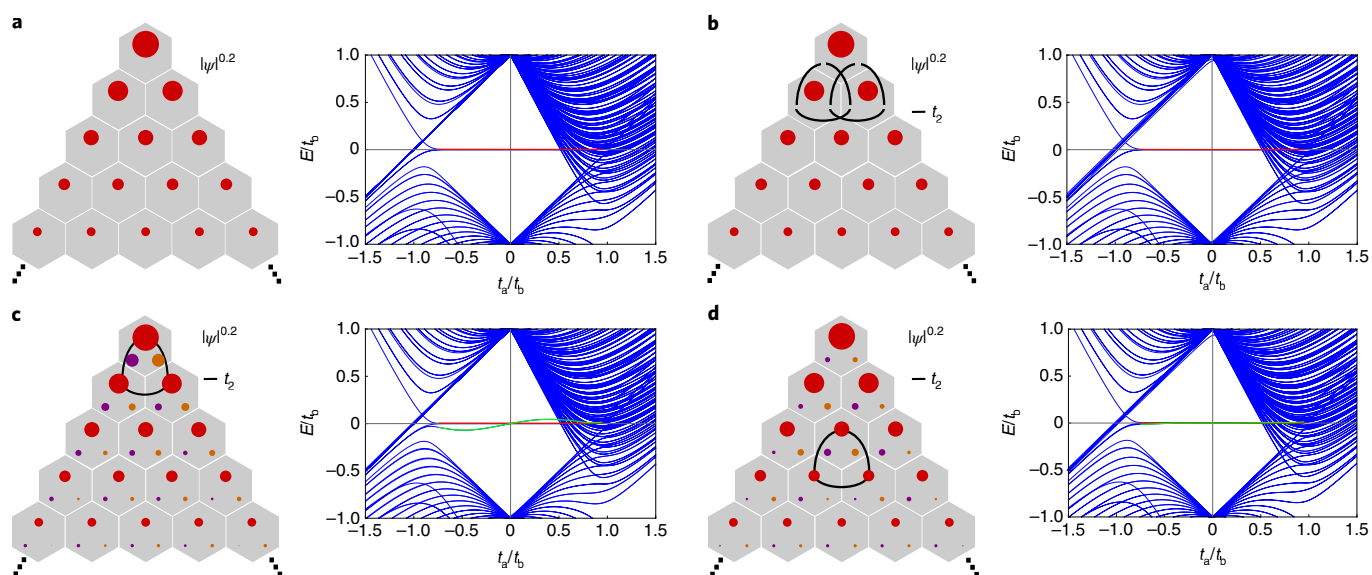
Fig. 3 | Robustness of the zero mode. a, Localization of the corner mode in the top of a kagome lattice containing 630 sites. The radius of the circles indicates $|\psi|^{0.2}$ to represent the decay of the wave function in a visible way, and the unit cells are indicated with grey hexagons. We use different colours to distinguish the sublattices (A is purple, B is orange and C is red). The corner modes exponentially localize on the corresponding sublattice C (see Supplementary Information). The spectrum is shown, where the zero modes are indicated with a red line (we set $\varepsilon = 0$ for simplicity in this calculation). **b**, Locally adding an NNN hopping term $t_2 = 0.05t_b$ between the A sublattice sites and a similar hopping term between the B sublattice sites breaks the generalized chiral symmetry for the top sites, but this does not affect the zero mode localized at sublattice site C. **c**, Breaking the chiral symmetry for the top sublattice site C shifts the zero mode to finite energy (green line) and the wave function no longer exponentially localizes only on the sublattice sites C. **d**, Breaking the chiral symmetry in the bulk also destroys the zero mode and the exponential localization, but the effect of this perturbation is less than in **c**. See the Supplementary Information for further analysis on the breaking of these symmetries.

moves away from zero energy and also decays in the A and B sub-lattices (see Fig. 3c). The other zero modes at the A and B corners of the lattice, nevertheless, remain unaffected. However, if the local perturbation in C is applied farther away from the corner mode, the disturbance is small (see Fig. 3d). Note that the generalized chiral symmetry is not broken by t_{nnn} and the orbital overlap that are present in the experiment (see Supplementary Information). These results indicate that the generalized chiral symmetry connected to a tripartite system offers more protection to the zero modes than usual bipartite systems do.

Finally, we show several examples of how these zero modes can also be created and destroyed experimentally by introducing defects into the lattice (see Fig. 4). The top CO molecule was shifted 0.256 nm upwards from its previous position, resulting in a small shift in ε (see Supplementary Information). In the following discussion, this shift is ignored. In the first defect realization, we remove the corner site at sublattice B (bottom-right corner) from the lattice by blocking the site with CO molecules (see Fig. 4a–d). Hence, one of the zero modes is no longer present (see Fig. 4a). The corner sites A and C are not affected by the defect, as shown in the differential conductance map at $V = +50$ meV in Fig. 4d. The generalized chiral symmetry is preserved for these modes, as their sublattices remain unperturbed. In this way, two zero modes remain by introducing a corner defect. Second, we append a protrusion at one edge, host-ing 120° obtuse angles, breaking the C_3 symmetry of the lattice but preserving one of its mirror symmetries (see Fig. 4e–h). We observe that the edge mode is disrupted around the positions where the edge no longer consists of only A and C sites (Fig. 4g). However, the corner modes remain unaltered under this perturbation (see Fig. 4h). This corroborates that the generalized chiral symme-try, being a local symmetry, offers a protection mechanism that is stronger than the one provided by crystalline symmetries: the zero-energy states persist even in the absence of crystalline

symmetries. Finally, a weakly connected site is added, breaking the mirror symmetry of the entire lattice, but preserving the generalized chiral symmetry. Again, the three zero-energy modes at the corners are resilient. Furthermore, the added weakly connected site at 60° (blue) exhibits a fourth zero-energy mode at sublattice A, protected by the generalized chiral symmetry. Hence, we show that it is pos-sible to create and/or destroy zero modes at will.

In fact, under the generalized chiral symmetry, zero modes exist whenever a site is only weakly connected to its neighbours (that is, connected to other sites by hopping terms of amplitude t_a, for $t_a < t_b$), as happens in all the cases where zero modes exist in Fig. 4. Only two zero modes that belong to different sublattices and that are in close proximity can hybridize to open a gap. If, however, zero modes belonging to the same sublattice are brought together, they will remain at zero energy. In this sense, the generalized chiral sym-metry provides a protection mechanism analogous to the conven-tional chiral symmetry in bipartite lattices, although in this case the existence of three species of zero modes offers more versatility.

The kagome lattice is known to be a fascinating system, mostly because it realizes geometric frustration and is conjectured to host the elusive spin–liquid phase. Here, we show that a breathing elec-tronic kagome lattice brings even further surprises. Protected zero modes arise at the corners of the lattice, thus realizing a HOTI with extreme robustness due to the tripartite character of the general-ized chiral symmetry. By introducing different types of defects into the lattice, zero modes can be manipulated at will, and one can tune the system to have an even or odd number of corner modes. The large degree of control over artificial lattices provides unique opportunities to study electronic topological phases. Our technique allows, in principle, the investigation of any breathing 2D lattice. Using the LDOS as a clear experimental observable, it is possible to detect symmetry-protected edge and corner modes not only at the Fermi energy but at all relevant energies of the model. The
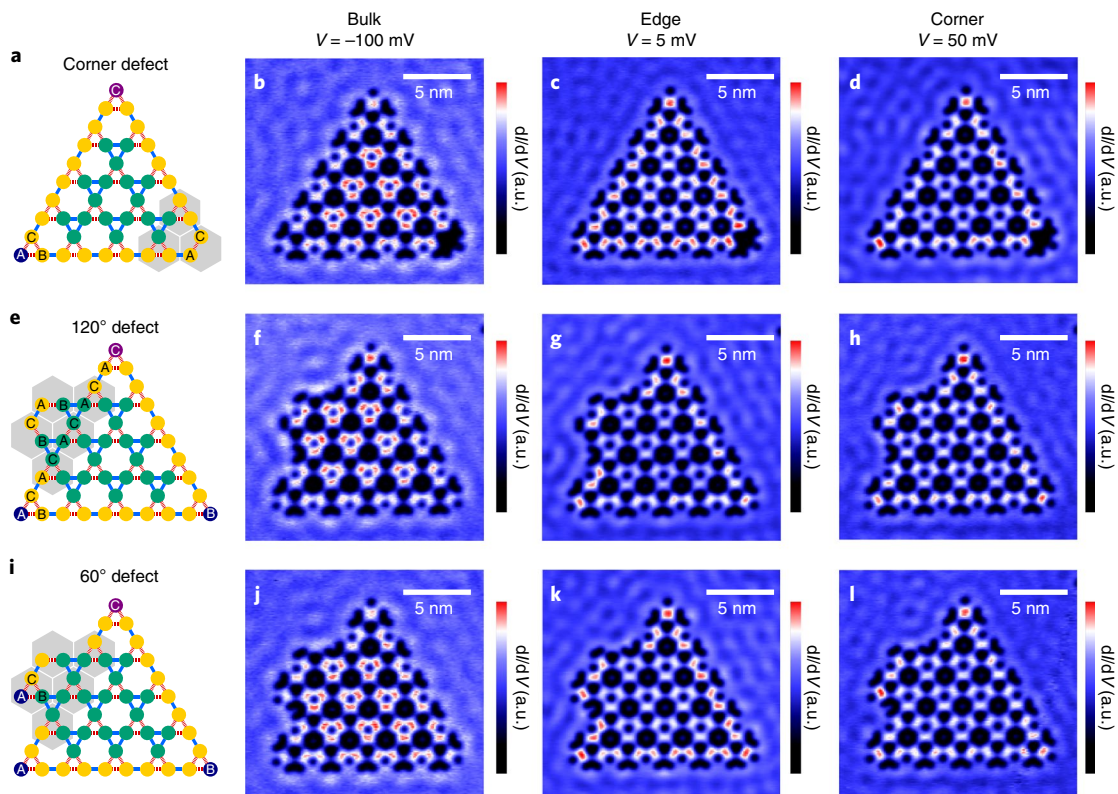
Fig. 4 | Boundary defects in the kagome lattice. a,e,i, Schematics of lattices from which a corner site was removed (**a**), with an appendix with two 120° angles added to one edge (**e**) and with one 120° and one 60° angle appended (**i**). The purple colour of the top site in the schematics indicates a slightly lower on-site energy, which is due to an upward shift of the top CO molecule by 0.256 nm. **b–d,f–h,j–l,** Differential conductance maps at $V = -100\,mV$ (bulk bands; **b,f,j**), $V = +5\,mV$ (edge bands; **c,g,k**) and $V = +50\,mV$ (corner states; **d,h,l**) for the three lattices.

protection mechanisms and robustness of topological phases can also be probed by selectively breaking certain symmetries. This can be done locally (for example, via introduction of atomically well-defined defects breaking the crystalline symmetry) or globally (for example, by applying a magnetic field). Furthermore, it will be possible to study the influence of disclinations. For topological crystalline insulators, the interplay of topologically protected edge modes and edge geometry can be probed. These electronic systems are thus complementary to photonic systems, which are designed on a much larger scale, and to the cold-atom set-ups, which offer great control but require nanokelvin temperatures for their operation. The progress in the realization of artificial electronic structures takes a step forward with the inclusion of topology among the parameters to be manipulated.

Online content

Any methods, additional references, Nature Research reporting summaries, source data, statements of code and data availability and associated accession codes are available at https://doi.org/10.1038/s41563-019-0483-4.

References

1. Feynman, R. P. There's plenty of room at the bottom. *Eng. Sci.* **23**, 22–36 (1960).
2. Georgescu, I. M., Ashhab, S. & Nori, F. Quantum simulation. *Rev. Mod. Phys.* **86**, 153–185 (2014).
3. Greiner, M., Mandel, O., Esslinger, T., Hänsch, T. W. & Bloch, I. Quantum phase transition from a superfluid to a Mott insulator in a gas of ultracold atoms. *Nature* **415**, 39–44 (2002).
4. Bloch, I., Dalibard, J. & Nascimbene, S. Quantum simulations with ultracold quantum gases. *Nat. Phys.* **8**, 267–276 (2012).
5. Blatt, R. & Roos, C. F. Quantum simulations with trapped ions. *Nat. Phys.* **8**, 277–284 (2012).
6. Aspuru-Guzik, A. & Walther, P. Photonic quantum simulators. *Nat. Phys.* **8**, 285–291 (2012).
7. Gomes, K. K., Mar, W., Ko, W., Guinea, F. & Manoharan, H. C. Designer Dirac fermions and topological phases in molecular graphene. *Nature* **483**, 306–310 (2012).
8. Crommie, M. F., Lutz, C. P. & Eigler, D. M. Confinement of electrons to quantum corrals on a metal surface. *Science* **262**, 218–220 (1993).
9. Hirjibehedin, C. F., Lutz, C. P. & Heinrich, A. J. Spin coupling in engineered atomic structures. *Science* **312**, 1021–1024 (2006).
10. Khajetoorians, A. A., Wiebe, J., Chilian, B. & Wiesendanger, R. Realizing all-spin–based logic operations atom by atom. *Science* **332**, 1062–1064 (2011).
11. Slot, M. R. et al. Experimental realization and characterization of an electronic Lieb lattice. *Nat. Phys.* **13**, 672–676 (2017).
12. Drost, R., Ojanen, T., Harju, A. & Liljeroth, P. Topological states in engineered atomic lattices. *Nat. Phys.* **13**, 668–671 (2017).
13. Slot, M. R. et al. *p*-band engineering in artificial electronic lattices. *Phys. Rev. X* **9**, 011009 (2019).
14. Collins, L. C., Witte, T. G., Silverman, R., Green, D. B. & Gomes, K. K. Imaging quasiperiodic electronic states in a synthetic penrose tiling. *Nat. Commun.* **8**, 15961 (2017).
15. Kempkes, S. N. et al. Design and characterization of electrons in a fractal geometry. *Nat. Phys.* **15**, 127–131 (2019).
16. Moore, J. E. The birth of topological insulators. *Nature* **464**, 194–198 (2010).
17. Haldane, F. D. M. Nobel lecture: topological quantum matter. *Rev. Mod. Phys.* **89**, 040502 (2017).
18. Hasan, M. Z. & Kane, C. L. Topological insulators. *Rev. Mod. Phys.* **82**, 3045–3067 (2010).
19. Benalcazar, W. A., Bernevig, B. A. & Hughes, T. L. Quantized electric multipole insulators. *Science* **357**, 61–66 (2017).
20. Noh, J. et al. Topological protection of photonic mid-gap defect modes. *Nat. Photon.* **12**, 408–415 (2018).
21. Schindler, F. et al. Higher-order topology in bismuth. *Nat. Phys.* **14**, 918–924 (2018).

22. Mittal, S. et al. Photonic quadrupole topological phases. *Nat. Photon.* https://doi.org/10.1038/s41566-019-0452-0 (2019).
23. El Hassan, A. et al. Corner states of light in photonic waveguides. Preprint at https://arxiv.org/abs/1812.08185 (2018).
24. Serra-Garcia, M. et al. Observation of a phononic quadrupole topological insulator. *Nature* **555**, 342–345 (2018).
25. Imhof, S. et al. Topolectrical-circuit realization of topological corner modes. *Nat. Phys.* **14**, 925–929 (2018).
26. Peterson, C. W., Benalcazar, W. A., Hughes, T. L. & Bahl, G. A quantized microwave quadrupole insulator with topologically protected corner states. *Nature* **555**, 346–350 (2018).
27. Xue, H., Yang, Y., Gao, F., Chong, Y. & Zhang, B. Acoustic higher-order topological insulator on a kagome lattice. *Nat. Mater.* **18**, 108–112 (2019).
28. Ni, X., Weiner, M., Alú, A. & Khanikaev, A. B. Observation of higher-order topological acoustic states protected by generalized chiral symmetry. *Nat. Mater.* **18**, 113–120 (2019).
29. Ezawa, M. Higher-order topological insulators and semimetals on the breathing kagome and pyrochlore lattices. *Phys. Rev. Lett.* **120**, 026801 (2018).
30. Benalcazar, W. A., Li, T. & Hughes, T. L. Quantization of fractional corner charge in C_n-symmetric higher-order topological crystalline insulators. *Phys. Rev. B* **99**, 245151 (2019).

Author contributions

S.N.K. and J.J.v.d.B. performed the theoretical calculations under the supervision of C.M.S., W.A.B. and D.B. M.R.S., S.N.K. and I.S. planned the experiment. M.R.S. performed the experiment and data analysis with contributions from P.C. under the supervision of I.S. and D.V. C.M.S., S.N.K. and M.R.S. wrote the manuscript with input from all authors.

Competing interests

The authors declare no competing interests.

Additional information

Supplementary information is available for this paper at https://doi.org/10.1038/s41563-019-0483-4.

Reprints and permissions information is available at www.nature.com/reprints.

Correspondence and requests for materials should be addressed to I.S. or C.M.

Publisher's note Springer Nature remains neutral with regard to jurisdictional claims in published maps and institutional affiliations.

Methods

Experiments. The STM and spectroscopy experiments were performed in a Scienta Omicron Low-Temperature STM system operating in sample-bias mode at a temperature of 4.5 K and a base pressure in the 10^{-11} mbar range. An atomically flat Cu(111) surface was prepared by several cycles of Ar^+ sputtering and annealing and was cooled in the STM head. CO molecules were leaked into the chamber for 20 min at a pressure of 1×10^{-8} mbar and adsorbed onto the cold surface. The kagome lattices were assembled and characterized using a Cu-coated platinum–iridium tip, prepared by gentle contact with the Cu(111) surface. CO manipulations were carried out in feedback at bias voltage $V = 20$ mV and current $I = 40$ nA, following previously reported procedures[31–33]. STM images were obtained in constant-current mode. Differential conductance spectra and maps were acquired in constant-height mode using a standard lock-in technique with a modulation amplitude of 10 mV root mean square at a frequency of 273 Hz.

Muffin-tin calculations. The muffin-tin model describes the surface-state electrons of the Cu(111) as a 2D electron gas confined between circular potential barriers (CO molecules) with a height of $V = 0.9$ eV and a radius $R = 0.3$ nm. The energy and wave functions for this model can be found by numerically solving the Schrödinger equation with this potential landscape. Due to the presence of the CO molecules, there is a non-zero probability for the surface state electrons to be scattered into bulk states of the copper, that is, the CO molecules induce a coupling between surface and bulk states. This reduces the lifetime and therefore increases the width of the peaks. To account for this effect, a broadening of $\Gamma = 0.08$ eV is included in the calculations.

Tight-binding calculations. The free electrons in the lattice act as though they are confined to certain artificial atom positions due to the placing of the CO molecules. We can describe this behaviour within a single-particle tight-binding model of connected s orbitals. The Thomas–Fermi screening length for Cu is 0.05 nm, and therefore the electron correlation effects can be ignored. By making a fit to the experimental and muffin-tin spectra, we are able to determine the hopping parameters, the on-site energy and the orbital overlap. We find the strong and weak hopping values (in the topological phase) $t_b = 0.075$ eV and $t_a = 0.38 t_b$. Furthermore, we obtain $t_{nnn} = 0.25 t_b$, $\varepsilon = 0.075$ eV and the orbital overlap between NNs $s_b = 0.22$ and $s_a = 0.9 s_b$. With these parameters, we solve the well-known generalized eigenvalue equation $H|\psi\rangle = E S |\psi\rangle$, where $\mathcal{S}$ is the overlap–integral matrix. Next, the LDOS is calculated at each atomic site, in which the broadening $\Gamma = 0.08$ eV is included to account for bulk scattering. Finally, the LDOS maps are calculated by multiplying the LDOS at each site with a Gaussian wave function of width $\sigma = 0.45d$, where $d = 1.33$ nm is the distance between two neighbouring sites.

Protection mechanism. The protection of the zero modes is due to an extension of the chiral symmetry. The conventional chiral symmetry is expressed as

$$\Gamma^{-1} h(\mathbf{k}) \Gamma = -h(\mathbf{k}) \tag{2}$$

where, without loss of generality, one can choose a basis in which the chiral operator Γ is a diagonal matrix with entries +1 for one sublattice and −1 for the other sublattice. In the breathing kagome lattice, we have an odd number of

lattice sites in the unit cell; therefore, the chiral symmetry does not hold. The concept, however, can be extended to a generalized version of the conventional chiral symmetry because the kagome lattice is tripartite. The generalized chiral operator Γ_3 can now be chosen (by an appropriate choice of ordering in the Hamiltonian matrix) to be a diagonal 3×3 matrix with entries $\Gamma_3 = \text{Diag}(1, e^{2\pi i/3}, e^{-2\pi i/3})$ that differentiates three sublattices[28]. The generalized chiral symmetry is then written as

$$\begin{aligned}
\Gamma_3^{-1} h_1(\mathbf{k}) \Gamma_3 &= h_2(\mathbf{k}), \\
\Gamma_3^{-1} h_2(\mathbf{k}) \Gamma_3 &= h_3(\mathbf{k}), \\
h_1(k) + h_2(k) + h_3(\mathbf{k}) &= 0
\end{aligned} \tag{3}$$

Using these equations, it can be shown that $\Gamma_3^{-1} h_3(\mathbf{k}) \Gamma_3 = h_1(\mathbf{k})$. If there is an eigenstate $|\psi_j\rangle$ that has support in only sublattice j, it will obey

$$\begin{aligned}
h_1 |\psi_j\rangle &= E |\psi_j\rangle \\
\Gamma_3 |\psi_j\rangle &= e^{i\theta_j} |\psi_j\rangle
\end{aligned} \tag{4}$$

for $\theta_j = \frac{2\pi}{3}(j-1)$, and $j = 1, 2, 3$. Using these expressions, we find from equation (3)

$$(h_1 + h_2 + h_3)|\psi_j\rangle = (h_1 + \Gamma_3^{-1} h_1 \Gamma_3 + \Gamma_3^{-2} h_1 \Gamma_3^2)|\psi_j\rangle = 0 \; (E + E + E)|\psi_j\rangle = 0 \tag{5}$$

from which it follows that $E = 0$ for any mode that has support only in one sublattice. We have verified numerically that all the modes for which we claim topological protection have support in only one sublattice (see Supplementary Information). In the topological phase, three zero modes exist simultaneously, each of which localizes at one of the three sublattices. This generalized chiral symmetry does not result in spectral symmetry of the bulk bands. Consequently, bulk bands can also have zero energy, but when the bulk bands are degenerate with the zero modes (for $1/2 < t_a/t_b < 1$) they do not mix with the localized corner zero modes. More details on the protecting symmetry and symmetry-breaking perturbations are given in the Supplementary Information.

Data availability

All data are available from the corresponding authors on reasonable request. The experimental data can be accessed using open-source tools.

References

31. Bartels, L., Meyer, G. & Rieder, K.-H. Basic steps of lateral manipulation of single atoms and diatomic clusters with a scanning tunneling microscope tip. *Phys. Rev. Lett.* **79**, 697–700 (1997).
32. Meyer, G. et al. Controlled manipulation of atoms and small molecules with a low temperature scanning tunneling microscope. *Single Mol.* **1**, 79–86 (2000).
33. Celotta, R. J. et al. Invited article: autonomous assembly of atomically perfect nanostructures using a scanning tunneling microscope. *Rev. Sci. Instrum.* **85**, 121301 (2014).